IEEE Photonics Journal
An IEEE Photonics Society Publication

Stress Engineering With Silicon Nitride Stressors for Ge-on-Si Lasers

Volume 9, Number 2, April 2017

Jiaxin Ke
Lukas Chrostowski
Guangrui Xia

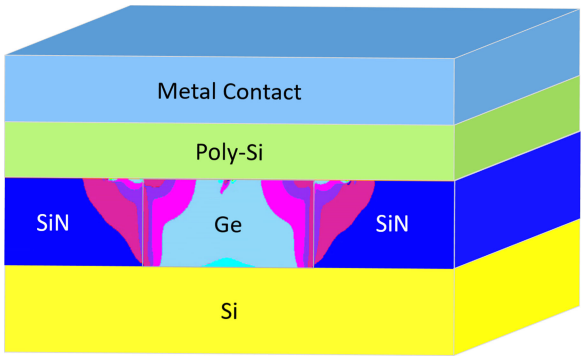

DOI: 10.1109/JPHOT.2017.2675401
1943-0655

IEEE photonics SOCIETY

IEEE

Stress Engineering With Silicon Nitride Stressors for Ge-on-Si Lasers

Jiaxin Ke,[1] Lukas Chrostowski,[2] and Guangrui Xia[1]

[1]Department of Materials Engineering, University of British Columbia, Vancouver, BC V6T 1Z4, Canada
[2]Department of Electrical and Computer Engineering, University of British Columbia, Vancouver, BC V6T 1Z4, Canada

DOI:10.1109/JPHOT.2017.2675401

Manuscript received January 27, 2017; accepted February 21, 2017. Date of publication March 2, 2017; date of current version March 29, 2017. This work was supported by the University of British Columbia.
Corresponding author: J. Ke (e-mail: kjxijk@gmail.com).

Abstract: Side and top silicon nitride stressors were proposed and shown to be effective in reducing the threshold current I_{th} and in improving the wall-plug efficiency η_{wp} of Ge-on-Si lasers. Side stressors only turned out to be a more efficient way to increase η_{wp} than using the top and side stressors together. With the side stressors and geometry optimizations, a η_{wp} of 34.8% and an I_{th} of 36 mA (J_{th} of 27 kA/cm^2) can be achieved with a defect limited carrier lifetime ($\tau_{p,n}$) of 1 ns. With $\tau_{p,n} = 10$ ns, an I_{th} of 4 mA (J_{th} of 3 kA/cm^2) and a η_{wp} of 43.8% can be achieved. These are tremendous improvements from the case with no stressors. These results give strong support to the Ge-on-Si laser technology and provide an effective way to improve the Ge laser performance.

Index Terms: Germanium, semiconductor lasers, silicon photonics

1. Background and Introduction

Optical interconnects are highly desired for on-chip and short-reach data communications to reduce the resistance-capacitor (RC) delay time and the power consumption. For this purpose, on-chip silicon (Si)-compatible light sources have long been pursued as electrical to optical signal converters, which are important and indispensable components of Si photonics. III-V semiconductor-based lasers integrated on Si via wafer bonding have provided the best performance so far, but they have the disadvantages of high cost, low yield, and low integration density, which are not suitable for mass production. The direct hetero-epitaxial growth of III-V materials on Si such as the InAs/GaAs quantum dots (QD) lasers demonstrated in [1] are more promising for low cost, high yield fabrication in the future. However, due to contamination issues, it will take a long time for III-V semiconductors to enter the mainstream Si fabrication facilities (fabs). Ge-on-Si laser is another competitive solution for the large-scale monolithic integration because it is fully compatible with the complementary metal-oixde-semiconductor field effect transistor (CMOS) technology, which may greatly reduce the process complexity, cost and time to enter the fabs [2]. Light emission from Ge by band engineering with tensile strains and high doping levels was theoretically predicted in 2007 [3]. The first optical pumped [4] Ge laser was first realized in 2010, and electrically pumped Ge lasers were demonstrated in 2012 [5] and 2015 [6] accordingly. Other types of Ge lasers like GeSn lasers [7], Ge QD lasers [8] have been demonstrated recently, which show the potential of Ge as a lasing material on Si. Unfortunately, the demonstrated Ge lasers suffer from high threshold current and low efficien-

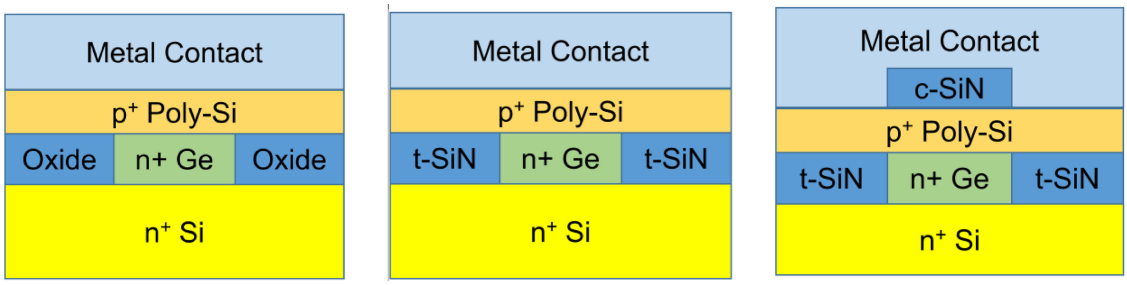

Fig. 1. Laser structure simulated (cavity width = 1 μm, thickness = 0.2 μm, length = 270 μm, cladding thickness = 0.18 μm). (a) Structure 1: without stressors. (b) Structure 2: with side nitride stressors. (c) Structure 3: with top and side nitride stressors. The width of the top nitride stressor is the same as that of the Ge cavity. The metal contacts are composed of Ti and Al, which are same as those in [5], shown in Fig. 2(a).

cies. The electrically pumped laser in [5] has a threshold current density (J_{th}) of 280 kA/cm^2, which is too high for any useful applications. Optimization of Ge lasers is in great need to lower the threshold current (I_{th}) and increase the efficiency. Bandgap engineering by stress is a very promising way to increase the gain [9] compared with higher doping because high doping introduces high optical loss. Introducing tensile strain to Ge can transfer Ge from an indirect bandgap material into a direct bandgap material and thus increase the gain [3], [10]. Both biaxial and uniaxial tensile strain can make this transition. Many efforts have been invested to increase the tensile strain in Ge. Sukhdeo *et al.* used a stress concentration method in Ge-on-insulator (GOI) substrates, and obtained 5.7% uniaxial tensile stress in Ge bridges [11]. G. Capellini *et al.* used silicon nitride layer to stress Ge up to about 1.5% uniaxial tensile strain, and the fabrication process was CMOS-compatible [12]. Simulation results showed that silicon nitride (SiN) top stressor could reduce I_{th} by two to three times [13]. A highly stressed Ge photodetector has been achieved to reach a detection range up to 1.8 μm [14].

Our previous simulation work showed that by adjusting the geometry of Ge cavity and increasing the cladding thickness, Ge laser's performance could be significantly improved [15]. To further enhance Ge laser performance, we used SiN stressors to introduce tensile strain in this work. Silicon nitride has been widely used in CMOS industry to introduce both tensile and compressive stress. The stress levels of SiN can be easily tuned by changing the deposition recipe. Intrinsic stress values of $\pm$2 Gpa were used in our simulations, which were achievable in CMOS technology [16]. SiN has a refractive index about 1.6 to 2. Therefore, it is suitable for the optical confinement too. Based on the MIT's experimental laser structure in [5], we proposed side and top nitride stressors to introduce stress in the Ge cavity. Three double-heterojunction Fabry-Perot laser structures were simulated to study the stressors' impact on the device performance (see Fig. 1). Structure 1 is the simplified version of the experimental laser structure in [5].

2. Laser Structures, Parameters Used and Calibration

Laser structures simulated in this work use MIT's experimental structure [5] as a start point. The cross section is illustrated in Fig. 2(a). The doping and the strain are the same as the experiments reported: Si substrate is 5×10^{19} cm^{-3} n-type doped; Ge is 4×10^{19}cm^{-3} n-type doped with 0.25% biaxial tensile strain; poly-Si is 3.6×10^{20} cm^{-3} p-type doped. In the simulations, 2 μm Si substrate was used. A virtual contact was defined underneath the bottom of the Si substrate and the top of metal layers for the biasing purpose. The structure was 1μm wide and 270 μm long with 180 nm thick poly-Si cladding layer. The thickness of Ge active layer was set to be 200 nm, which was the average value of the 100$\sim$300 nm thickness in the experiments due to the process non-uniformity [5], [17].

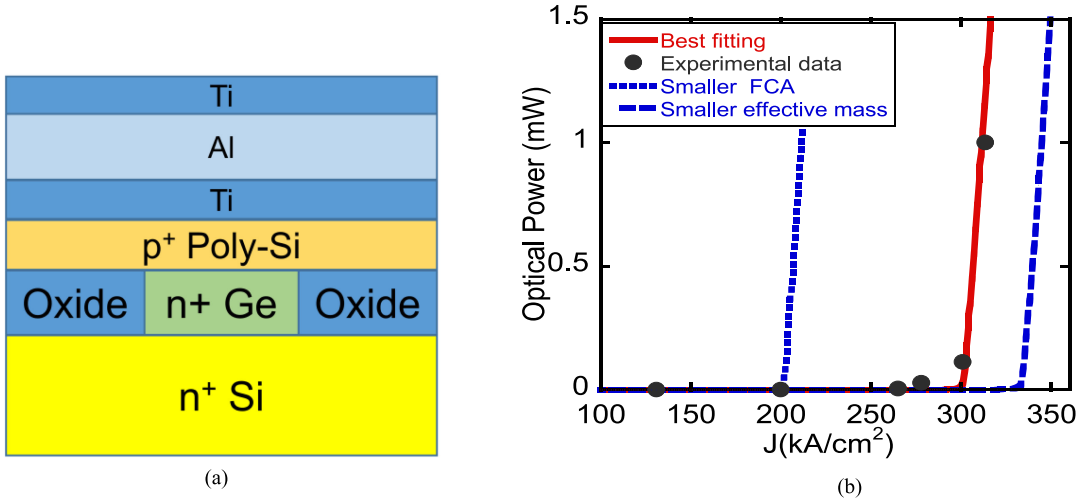

Fig. 2. (a) Cross-section of the Ge-on-Si heterojunction laser structure simulated. (b) L-I curves for experimental result, calibration result, and sensitivity tests with a smaller FCA coefficient for holes: $\alpha_i = 5.0 \times 10^{-19} N + 0.923 \times 10^{-17} P$, and a smaller effective mass $m_{e\Gamma*} = 0.045335\, m_e$.

The strain-dependent Ge energy bandgap model in [18], [19] and the doping induced bandgap narrowing effect [20] were implemented in a commercial 2D laser simulation tool LASTIP™. The metal-semiconductor heterojunctions were aligned by electron affinity as described in [25]. The reflectivity values of two facet are $R_1 = 23\%$ and $R_2 = 38\%$, which correspond to a mirror loss α_m of 45 cm^{-1} [21]. Auger coefficients used were $C_{nnp} = 3.0 \times 10^{-32} cm^6/s$ and $C_{ppn} = 7.0 \times 10^{-32} cm^6/s$ [3], [17]. The index of refraction values of all materials were wavelength dependent. The material parameters used mainly come from [5] and [15]. Surface recombination was not included in our simulations because of the unavailability of the relevant data of the Ge in the experiment. 1 ns of defect limited carrier lifetime ($\tau_{p,n}$) was used as a conservative estimation [22].

For the optical loss, we assumed that the internal loss and mirror loss is the primary sources of the loss and internal loss is dominated by the free carrier absorption [23]. In LASTIP™, for a narrow wavelength range, the free carrier absorption is described by $\alpha_i = AN + BP$, where A, B are constants and N, P are the electron and hole density in the unit of cm^{-3}. We used the first principle calculations results of free carrier absorption in n-type doped Ge for n-loss coefficient $A = 5.0 \times 10^{-19}$ [17] and the experimental measurement results in p-type doped Ge [24] as a starting point to obtain the best fitting to the L-I curve in [5]. The effective mass of gamma conduction band ($m^*_{e\Gamma}$) was used as the first fitting parameter of L-I curve. This is because that in reality, Si-Ge interdiffusion happens at Ge/Si interface during Ge growth, defect, and dopant activation annealing. N-type dopants enhance this interdiffusion greatly. The active region cannot be considered as a pure Ge, but a region with some Si diffused from the substrate [28], [29]. Compared to other parameters such as band structure, $m^*_{e\Gamma}$ has a stronger dependence on the Si molar fraction in the intermixed region due to the large effective mass difference between Si and Ge. As the Ge profile in the MIT experiment was not calibrated [17], and the simulation tool was not able to include the Ge concentration change, we were not able to determine $m^*_{e\Gamma}$ as a function of z position. Instead, we used $m^*_{e\Gamma}$ as a fitting parameter, and it had a big impact on the L-I behavior (see Fig. 2(b)). The p-loss coefficient B was used as the second fitting parameter. The best fitting was obtain when $m_{e\Gamma^*} = 0.045735 m_e$ and the best fitting free carrier loss relation was $\alpha_i = 5.0 \times 10^{-19} N + 1.023 \times 10^{-17} P$.

Using these parameters, our model produced J_{th} of 300 kA/cm^2 or I_{th} of 800 mA at 15 °C with the transverse electric (TE) mode lasing at $\lambda = 1676$ nm, which were very close to the experimental values of $J_{th} = 280\, kA/cm^2$ and lasing wavelength of 1650 nm [5]. As seen in Fig. 2(b), the model could match the experimental L-I curve quite well. Sensitivity test results are shown in Fig. 2(b),

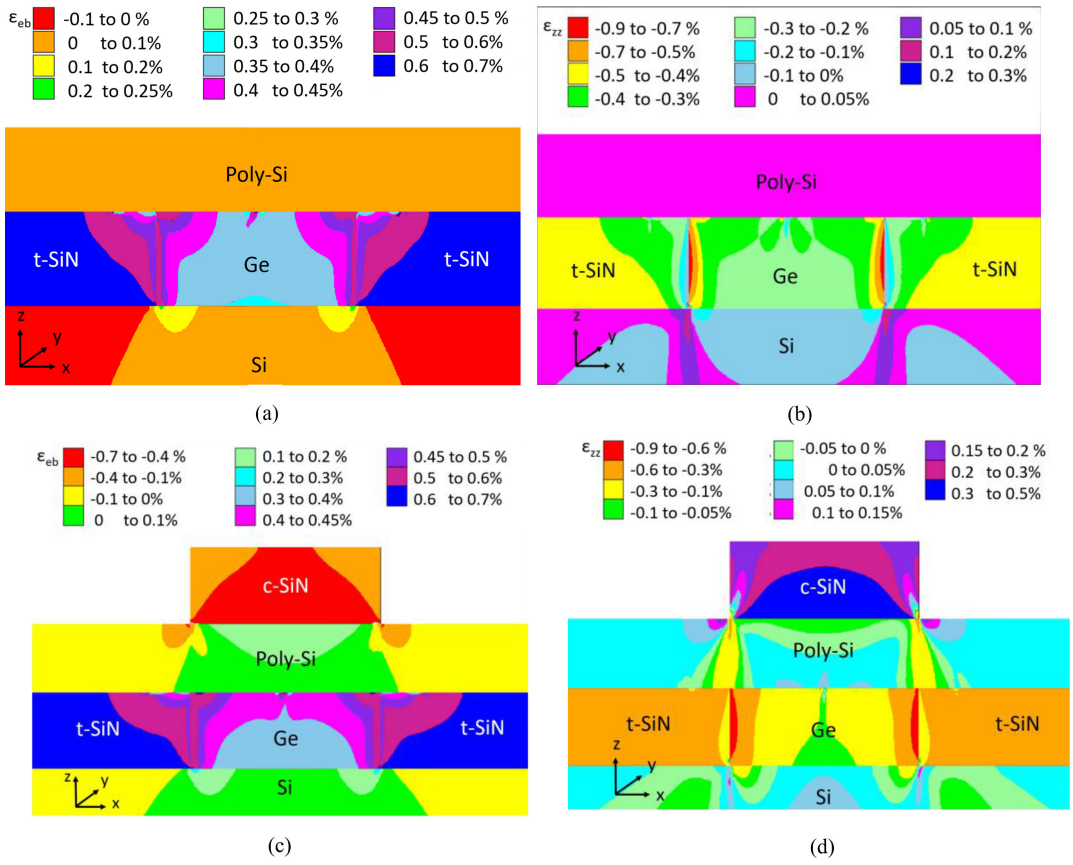

Fig. 3. Two-dimensional Strain map on the cross section. (a) ε_{eb} (b) ε_{zz} of structure 2 with side stressors only and (c) ε_{eb} (d) ε_{zz} of structure 3 with side and top stressors. (For both structures, cavity width $=$ 1 μm, thickness $=$ 0.2 μm, and cladding thickness $=$ 0.18 μm).

which shows how a smaller FCA parameter or a smaller $m^*_{e\Gamma}$ are not fitting the experimental data. After the calibration of our model, we started optimizing the laser structure.

3. Strain Calculations and Impact on Laser Performance

The stress and strain simulations were performed using a standard two-dimensional (2D) process simulation tool TSUPREM-4. For strain introduced by SiN stressors, a plane strain assumption (strain in length direction $\varepsilon_{yy} = 0$) is suitable as the length dimension in y direction is much longer than the width and thickness dimensions. Ge's Young's modulus and Poisson ratio used were 102 Gpa and 0.28 respectively. A Young's modulus of 200 Gpa in [30] was used for silicon nitride and the Poisson ratio used was 0.24. The intrinsic stress values used for tensile silicon nitride (t-SiN) and compressive silicon nitride (c-SiN) were $+2$ and -2 GPa respectively. A tensile strain value of 0.25% in Ge resulted from the thermal expansion mismatch between Ge and Si in ε_{xx} and ε_{yy} was included in the simulations. Since ε_{xx} and ε_{yy} appear in the form of $\varepsilon_{xx} + \varepsilon_{yy}$ in the strain-dependent bandgap models, it is reasonable to use effective biaxial strain $\varepsilon_{eb} = \frac{(\varepsilon_{xx}+\varepsilon_{yy})}{2}$ to represent the in-plane strain magnitude for the following discussions. The average value of ε_{eb} in center line was used to represent the strain field for simplification. ε_{xx}, ε_{yy}, and ε_{zz} were then loaded into LASTIP for the device simulation.

Structure 2 and 3 have the same cavity sizes as those in MIT's experiments but with the SiN stressors as illustrated in Fig. 1(b) and (c). Strain maps of ε_{eb} and ε_{zz} of both structures are illustrated in Fig. 3. Significant ε_{eb} were introduced by the stressors as shown in the strain map (see Fig. 3(a)

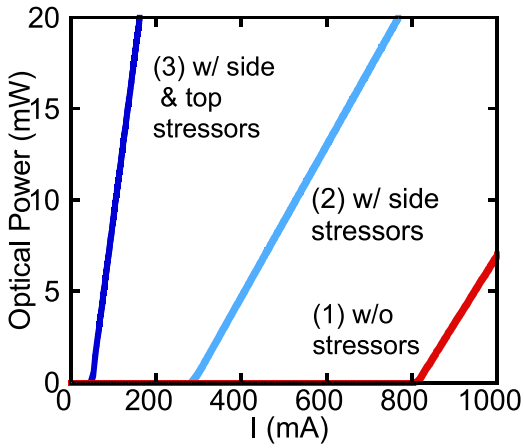

Fig. 4. L-I curve comparison for the three structures in Fig. 1 before the structure optimizations.

TABLE I
Laser Performance of the Three Structures in Fig. 4

Structure	1	2	3
ε_{eb}	0.25%	0.36%	0.39%
I_{th} (mA)	810	287	49
η_d	6.33%	7.20%	31.94%
highest achievable η_{wp}	2.07%	3.12%	16.03%

and (c)). With only side stressors, 0.36% ε_{eb} was introduced including the 0.25% strain caused by the thermal expansion mismatch. The value was increased to 0.39% by adding a top stressor. This strain enhancement is not optimized due to the non-optimized Ge width and thickness as the stress introduction strongly depends on the stressor and the cavity's sizes and relative positions. Compared to Structure 1, by adding the side stressors, about 523 mA reduction in I_{th} and 1.05% increase in η_{wp} were obtained. By adding the top and side stressors, about 761 mA reduction in I_{th} and 14% growth in η_{wp} were obtained (see Fig. 4 and Table I). The significant performance improvement introduced by the top stressors is because that top stressor not only introduces higher stress but also decreases the optical loss caused by the metal contact and provides optical confinement in the vertical direction.

4. Laser Structure Optimization Methodology and Structure 2 Optimizations

To take the full advantage from the stressors and further improve the device performance, we optimized the Ge cavity and the cladding geometry. We chose W, d_{Ge}, and d_{poly} as the parameters to be optimized, which stand for the Ge cavity width, thickness, and the poly-Si cladding layer thickness respectively. The Ge cavity length was set to be unchanged at 270 μm. In our optimization process, the goal is not to find the "true" optimal point, but rather to show that Ge lasers can be improved significantly. The reasons for that are two-fold. 1) Ge is not a well-studied optical material, and many model parameters do not have widely agreed values or even ranges. Therefore, it is still too early to find the "true" optimal at this point. 2) Optimizing one variable at a time is more

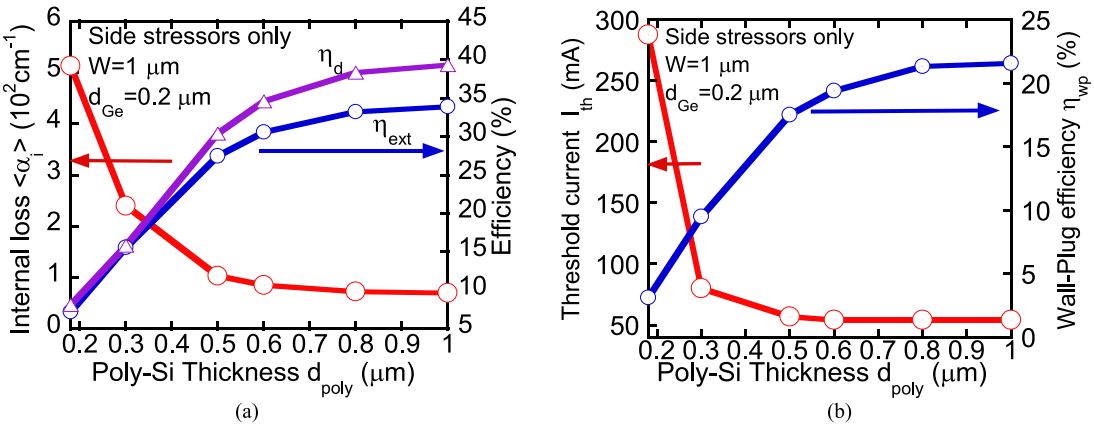

Fig. 5. Poly-Si thickness d_{poly} dependence (W = 1 μm, d_{Ge} = 0.2 μm) of (a) $<\alpha_i>$ and η_{ext}, η_d and (b) I_{th} and η_{wp}.

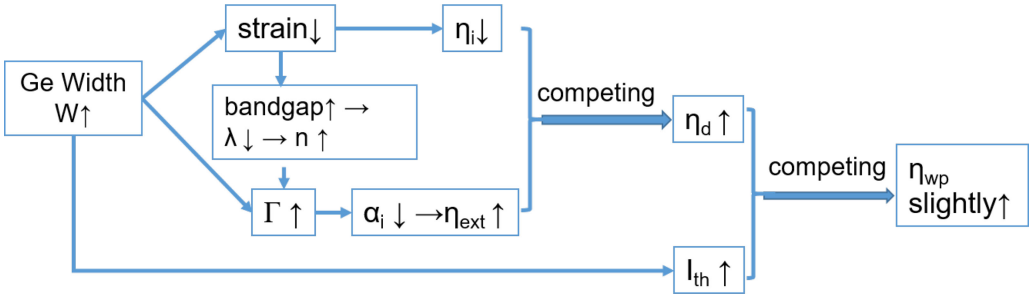

Fig. 6. Impacts of Ge Width (W) to other parameters.

doable, as the rate equations are well established, and one can check the correctness of the results conveniently.

Laser rate equations below were used to analyze the results. Slope efficiency η_d is calculated from (1), where $\Delta P/\Delta I$ is the slope of L-I curve, c is the speed of light, and h is the Planck's constant. η_d is the product of the internal efficiency η_i and the extraction efficiency η_{ext}. $<\alpha_i>$ in (2) is the weighted average of the local loss. $R_{srh}(n_{th}, p_{th})$ and $R_{Aug}(n_{th}, p_{th})$ are the non-radiative recombination coefficients due to traps and Auger process respectively. $R_{rad}(n_{th}, p_{th})$ is the spontaneous recombination rate. W and d are the thickness and width of Ge cavity respectively. η_{wp} is defined here as the max wall-plug efficiency that can be achieved. Two-dimensional laser L-I and I-V simulations were performed up to about 10 mW optical output, above which, to save computation time, L-I and I-V curves were extrapolated linearly up to about 200mW optical output, based on which the maximum η_{wp} was determined.

$$\eta_d = \frac{\Delta P}{\Delta I} \Big/ \frac{hc}{q\lambda} = \eta_i \frac{\alpha_m}{<\alpha_i> + \alpha_m} = \eta_i \eta_{ext} \tag{1}$$

$$\eta_{ext} = \frac{\alpha_m}{<\alpha_i> + \alpha_m} \tag{2}$$

$$I_{th} = \frac{qdW}{\eta_i} \left(R_{srh}(n_{th}, p_{th}) + R_{rad}(n_{th}, p_{th}) + R_{Aug}(n_{th}, p_{th}) \right) \tag{3}$$

$$\eta_{wp} = \text{Max} \left[\frac{P_{op}}{I \cdot V} \right]. \tag{4}$$

In most of our optimizations, we changed one parameter at a time and kept others unchanged, except for the case of Structure 3, where both top and side stressors were optimized together (see

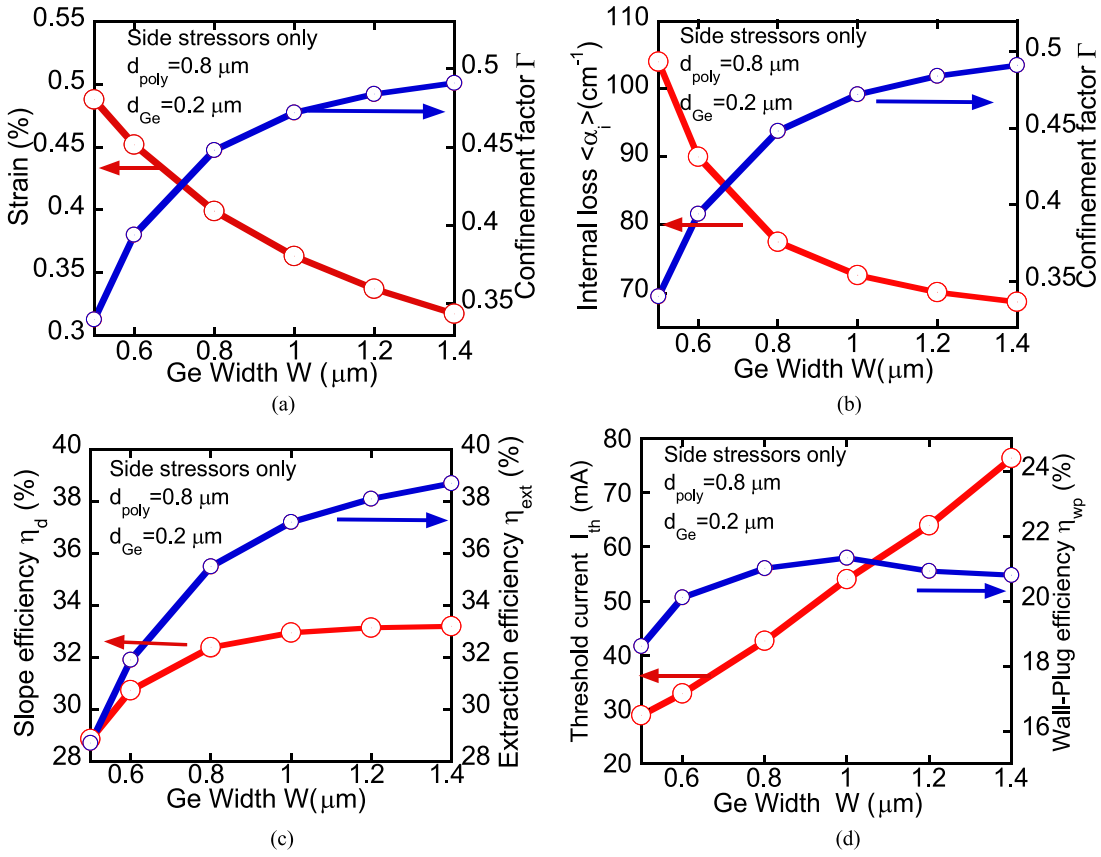

Fig. 7. Ge Width W dependence ($d_{poly} = 0.8\,\mu$m, $d_{Ge} = 0.2\,\mu$m) of (a) strain ε_{eb} and Γ, (b) $<\alpha_i>$ and Γ, (c) η_d and η_{ext}, and (d) I_{th} and η_{wp}.

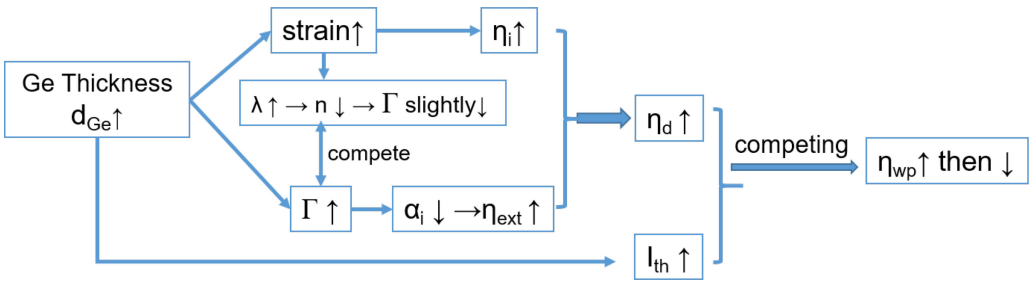

Fig. 8. Impacts of Ge thickness d_{Ge} to other parameters.

details in Section 5.3). Next, we will use Structure 2 as an example to illustrate the optimization process. For lasers, small I_{th} and large η_{wp} are both desired, but they may not be met at the same time. We chose η_{wp} as the most important optimization criteria because it represents the energy efficiency of the device.

4.1 Poly-Si Thickness d_{poly} Optimizations

The poly-Si thickness d_{poly} has the most dominant effect in the geometry optimization. As d_{poly} increased, we observed a dramatic increase in η_{wp} and a decrease in I_{th}. These improvements are because that the metal is very lossy optically. As the top metal contact moved further away

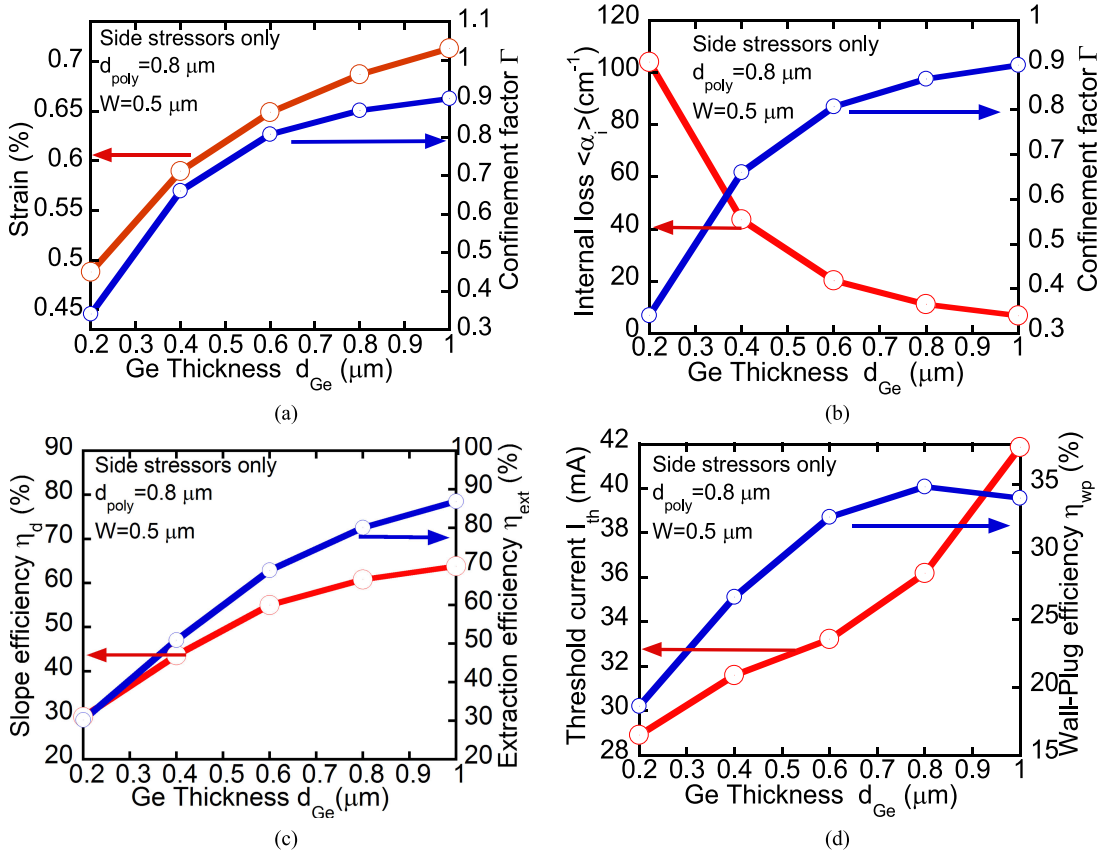

Fig. 9. Ge thickness d_{Ge} dependence (W = 0.5 μm, d_{poly} = 0.8 μm) of (a) strain ε_{eb} and Γ, (b) $<\alpha_i>$ and Γ, (c) η_d and η_{ext}, and (d) I_{th} and η_{wp}.

from the Ge cavity with the increase in d_{poly}, $<\alpha_i>$ caused by the metal contact decreases. As a result, η_{ext} and thus η_d increase monotonically and plateau at thick d_{poly} (see Fig. 5(a)). I_{th} decreases as d_{poly} increases since less carrier density is needed to compensate for the loss. As a consequence, η_{wp} increases to 21.3% and plateaus after $d_{poly} = 0.8\,\mu$m and I_{th} decreases to 54 mA (see Fig. 5(b)). We chose 0.8 μm as the optimization point since η_{wp} plateaued after that point.

4.2 Ge Width W Optimizations

The W and d dependence come from three different effects: 1) strain introduction, 2) optical confinement factor Γ and 3) active region volume. The relationship between different parameters is shown in Fig. 6. The tensile strain decreases with the increase of W because side stressors are moved away from the center (see Fig. 7(a)). The separation between the direct and indirect band gap increases accordingly, which results in a reduction in η_i. The decrease in strain raises the bandgap, causing the lasing wavelength to become smaller. The reduced lasing wavelength causes a slight increase in the refractive index and thus increases Γ. As the cavity becomes wider, the lateral confinement becomes better, which also increases Γ (see Fig. 7(a)). The FCA loss of poly-Si is bigger than Ge. So a bigger Γ means fewer light travels in the lossy poly-Si region, which results in the decrease of $<\alpha_i>$ and the increase of η_{ext} and thus the growth of η_d (see Fig. 7(b) and (c)). I_{th} is a combination effect of n_{th}, η_i, and geometry as indicated in Eq. (3) but mostly dominated by geometry since I_{th} increases almost linearly with W in Fig. 7(d). The bigger the W is, the larger current is needed to compensate the carrier loss resulted mainly from R_{srh} and R_{Aug}.

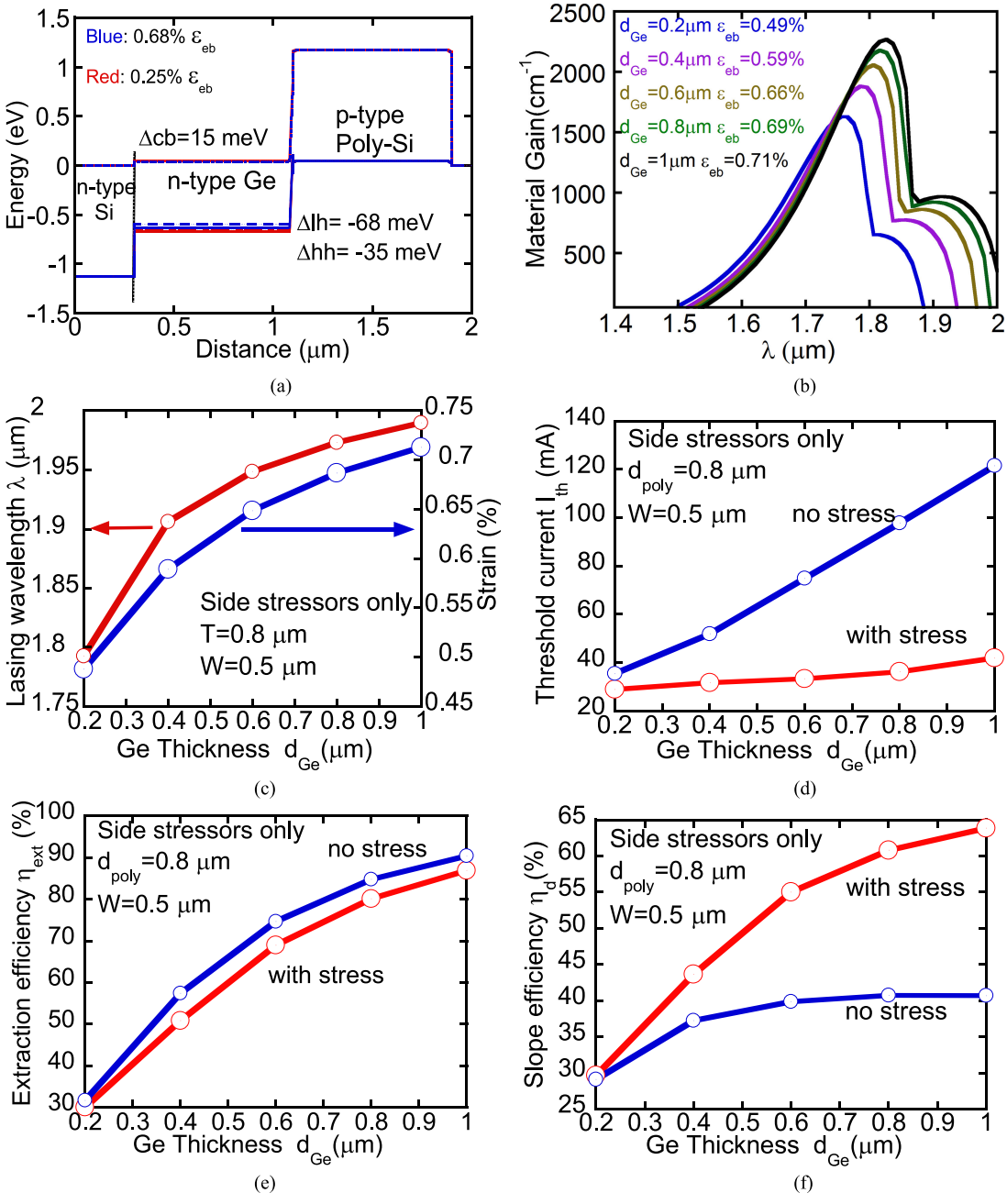

Fig. 10. Strain impact with different d_{Ge} ($W = 0.5\mu m$, $d_{poly} = 0.8\ \mu m$). (a) Direct band alignment under and without stressor's strain ($d_{Ge} = 0.8\,\mu m$). (b) Material gain at different strain with carrier concentration $n = p = 4\times10^{19}cm^{-3}$. (c) Strain ε_{eb} and λ. (d) η_{ext}. (e) I_{th}. (f) η_d.

The increase of η_d would increase η_{wp} whereas increased I_{th} would decrease it. Because of the competing effect, η_{wp} only increases slightly with W as shown in Fig. 7(d). Further simulations show that choosing the maximum η_{wp} point where $W = 1\ \mu m$ does not promise better performance in d dependence since a narrower waveguide is desired for side stressors. On the contrary, a wider cavity increases I_{th} greatly. Therefore, we chose $W = 0.5\ \mu m$ as the optimization point, where $\eta_{wp} = 18.61\%$ now but promotes the potential for higher efficiency.

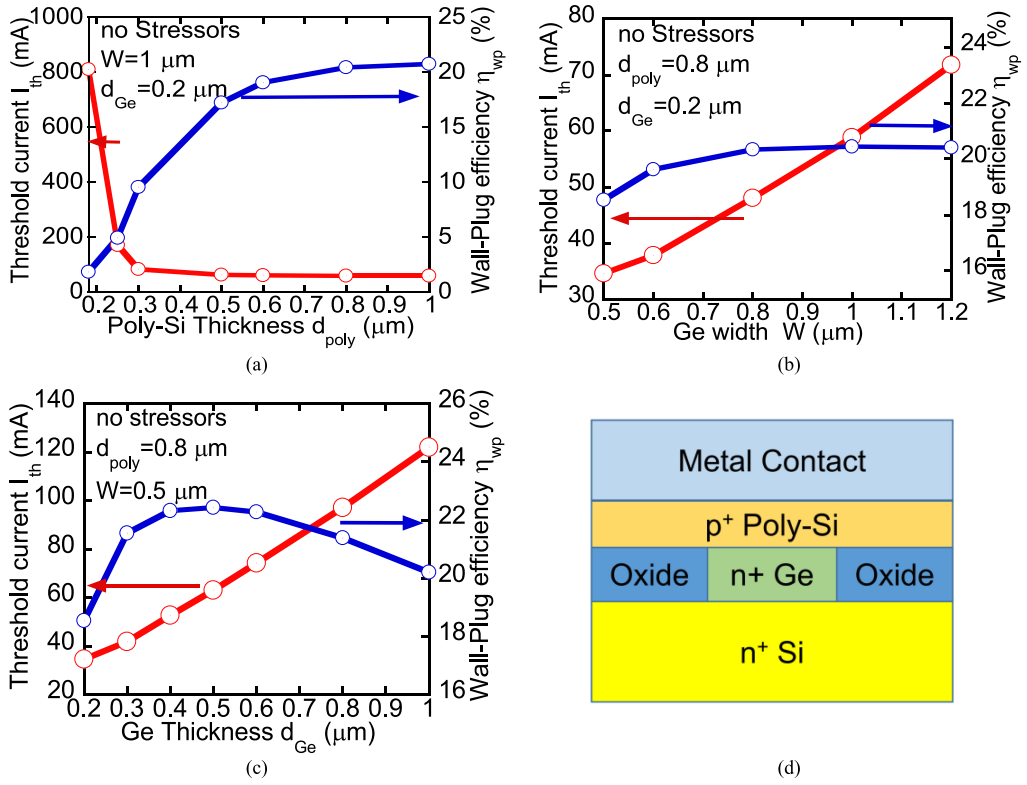

Fig. 11. I_{th} and η_{wp} of Structure 1. (a) d_{poly} dependence. (b) Width dependence. (c) d_{Ge} dependence. (d) Cross section of Structure 1.

4.3 Ge Thickness d_{Ge} Optimizations

The dependence of d_{Ge} is similar as W's dependence, which is shown in Fig. 8. Strain and η_i increase with d_{Ge} because more stressors react on the Ge cavity (see Fig. 9(a)). Γ increases with d_{Ge} since thicker cavity promote better vertical confinement (see Fig. 9(a)). The Γ shrinkage due to the change of lasing wavelength is only a minor effect for Γ. The increase in Γ causing the $<\alpha_i>$ to shrink and thus increase the η_{ext} (see Fig. 9(b) and (c)). As a result, η_d increases a lot since η_i and η_{ext} are of same trend (see Fig. 9(c)). Same as the W dependence, I_{th} increases almost linearly with d_{Ge} (see Fig. 9(d)). As the competing effect of I_{th} and η_d, η_{wp} peaks at 34.8% and then decreases (see Fig. 9(d)). We chose $d_{Ge} = 0.8\,\mu$m as the optimization point.

By comparing the same structure in d_{Ge} dependence with and without stressors, we can see how strain influences the laser performance. Increased strain decreases the difference between gamma (direct) and L (indirect) conduction band (not shown here), decreases the bandgap and increases the gap between lh and hh band (see Fig. 10(a)). These changes in band increase the material gain (see Fig. 10(b)), which decreases the carrier density needed for lasing and thus reduce I_{th} (see Fig. 10(d)). The increased lasing wavelength (see Fig. 10(c)) decreases Γ by the changed real index n and decreases η_{ext} slightly as discussed before (see Fig. 10(e)). The η_d increases while η_{ext} decreases by the decreased Γ, which shows that the η_i increases with the strain for the same geometry (see Fig. 10(f)).

5. Structure 1 and 3 Optimizations and Comparisons Between Structures

5.1 Optimizations of Structure 1 Without Stressors

For Structure 1, without the stressors, the trend is similar to Structure 2, as shown in Fig. 11, but with lower η_{wp}. d_{poly} had the largest impact and was first optimized as in Fig. 11(a). I_{th} decreases

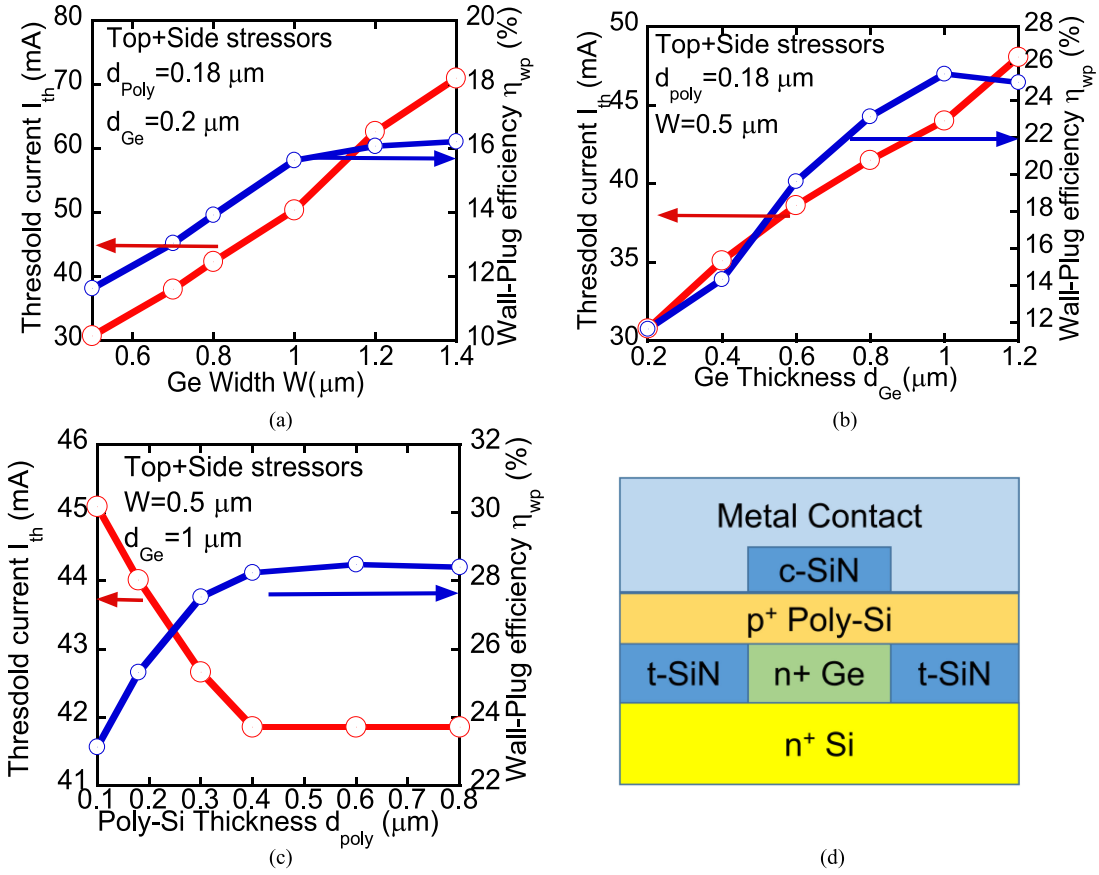

Fig. 12. I_{th} and η_{wp} of Structure 3. (a) Width dependence. (b) d_{Ge} dependence. (c) d_{poly} dependence. (d) cross section of Structure 3.

from 810 to 57 mA and η_{wp} increases from 2.07% to 20.8% when d_{poly} changes from 0.2 to over 0.8. We chose $d_{poly} = 0.8\ \mu$m as the optimized d_{poly}. For the W dependence, I_{th} increases linearly with W, but η_{wp} does not change much with W (see Fig. 11(b)). So we chose $W = 0.5\ \mu$m as the optimized W for less I_{th}. We chose the peak point $d_{Ge} = 0.5\ \mu$m as the optimization point for d_{Ge} dependence. The highest efficiency reached is 22.4% with $d_{poly} = 0.8\ \mu$m $W = 0.5\ \mu$m, $d_{Ge} = 0.5\ \mu$m $I_{th} = 63$ mA.

5.2 Optimization Summary of Structure 2 With Side Stressors Only

Detailed geometry dependence and the optimized process were discussed in 4.1-4.3. After the optimizations, the highest η_{wp} achievable is 34.84%, and an I_{th} of 36 mA with $d_{poly} = 0.8\ \mu$m $W = 0.5\ \mu$m, $d_{Ge} = 0.8\ \mu$m.

5.3 Optimizations of Structure 3 With Top and Side Stressors

Due to the presence of the top stressor, the top metal contact loss is greatly reduced for Structure 3 before increasing d_{poly}. A large W and small d_{Ge} are desired for the strain introduction from the top stressor, which is undesired for the side stressors. Therefore, W and d_{Ge} are optimized together to obtain a high η_{wp}. $W = 0.5\ \mu$m is not the optimized width in Fig. 12(a), but by comparing a few different W values, $W = 0.5\ \mu$m has the potential to produce a higher η_{wp}. $d_{Ge} = 1\ \mu$m is the optimization point of d_{Ge} dependence for $W = 0.5\ \mu$m. For such structures, the strain introduction from side stressors is more prominent than the top stressor. d_{poly} has similar but weaker

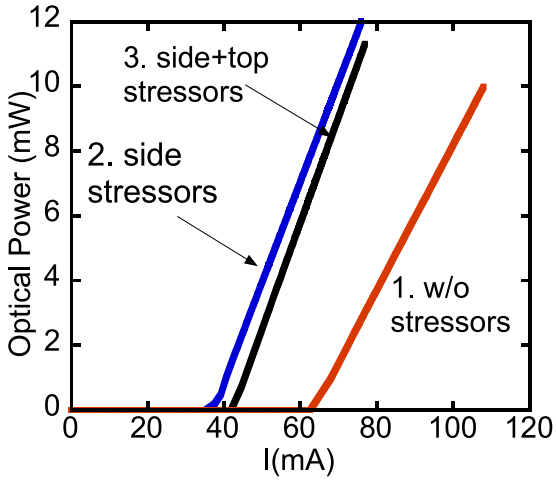

Fig. 13. L-I curve for three structures after optimization.

TABLE II
Laser Performance of the Three Structures in Fig. 13 After Structure Optimizations

Structure	1	2	3
ε_{eb} (%)	0.25	0.713	0.714
I_{th} (mA)	63	36	42
J_{th} (kA/cm^2)	47	27	31
η_d (%)	38.6	60.8	61.9
highest η_{wp} (%)	22.4	34.8	28.3
Current required for highest η_{wp}(mA)	494	270	210
Output power at highest η_{wp} (mW)	100	72	55

impact compared to Structure 2. The increasing d_{poly} would further increase η_{wp} and decrease I_{th}, which shows that top stressor can only diminish the optical loss caused by metal to a certain extent. Increasing d_{poly} is a more efficient way to reduce the optical loss. The final optimization is $d_{poly} = 0.4\,\mu$m, W $= 0.5\,\mu$m, $d_{Ge} = 1\,\mu$m, with η_{wp} peaks at 28.3% and an I_{th} of 42 mA.

5.4 Comparisons of the Structures

The comparisons of the three structures after optimization are shown in Fig. 13 and Table II. We can observe that changing geometry could significantly increase η_{wp} and decrease I_{th}. Adding stressors can further improve them. By using side stressors only, the highest η_{wp} rose to 34.8%, but adding top stressor does not provide greater η_{wp}. This is mainly because that the top stressor increases the series resistance significantly. Structure 1 and 2 have a series resistance around 0.4 Ω, but it is around 0.9 Ω for Structure 3, which means Structure 3 requires higher voltage and thus higher electric power. Plus, the strain introduced by top stressor is marginal compared to side stressors. As a result, Structure 3 does not produce a higher η_{wp} than Structure 2. Therefore, considering both η_{wp} and I_{th}, Structure 2, with side stressors only, is recommended.

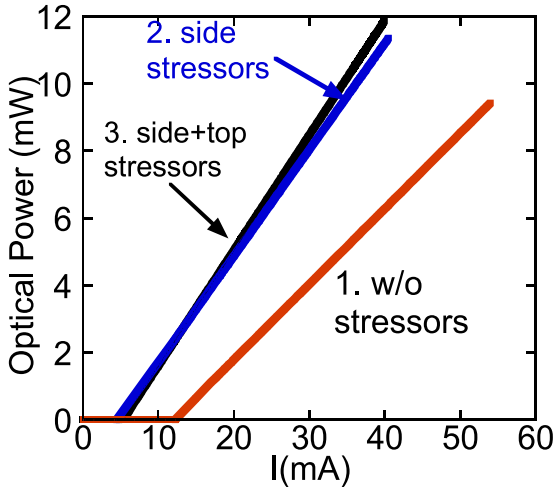

Fig. 14. L-I curve for three structures with $\tau_{p,n} = 10$ ns.

TABLE III
Laser Performance of the Three Structures in Fig. 14

Structure	1	2	3
ε_{eb} (%)	0.25	0.713	0.714
I_{th} (mA)	12	4	5
J_{th} (kA/cm^2)	8.8	3.0	3.7
η_d (%)	38.7	62.3	64.8
highest achievable η_{wp} (%)	27.0	43.8	41.1
Current required for highest η_{wp} (mA)	167	81	55
Output power at highest η_{wp} (mW)	35	24	17

6. Defect-Limited Minority Carrier Lifetime Dependence

For the study above, the defect-limited minority carrier lifetime $\tau_{p,n}$ is set as 1ns for conservative prediction. It is used for Shockley–Read–Hall (SRH) recombination rate calculation, which is defined by: $\tau_{p,n} = \frac{1}{\sigma_{p,n} N_t v_{p,n}}$ in which $v_{p,n}$ is the thermal velocity of hole and electron and $\sigma_{p,n}$ is the effective capture cross-section of the deep defect state traps. For simplicity, a default setting in the software was used: we assumed that τ_p and τ_n are the same and a uniform distribution of donor mid-gap traps with a density of 10^{10} m^{-3}. Capture coefficients $c_{p,n} = \sigma_{p,n} v_{p,n}$ are calculated from the relationship of $\tau_{p,n}$ above and then used in the calculation of SRH recombination rate R_{SRH}.

Fig. 14 and Table III show the performance of the 3 structures with $\tau_{p,n} = 10$ ns. From the results, we can see that by improving the material quality, the performance of laser could improve greatly. I_{th} decreases about 5-10 times when $\tau_{p,n}$ increases from 1ns to 10ns. Longer carrier lifetime means carrier decays slower in the cavity and thus less injection carrier is needed for lasing, which reduces I_{th} accordingly. It increases the highest η_{wp} by around 10% for structures with stressors and it decreases the current needed to reach that point significantly. Technically, it is feasible to obtain Ge layers with better quality and longer carrier lifetime by approaches like Ge growth on a GOI substrate [26] or direct wafer bonding and chemical mechanical polishing (CMP)

[27]. Defect-limited minority carrier lifetimes of 5.3 and 3.12 ns have been achieved respectively by the above approaches [26], [27]. Therefore, if a better material quality can be achieved, along with the geometry and stress engineering, Ge laser performance will not be too far from III-V lasers.

7. Conclusion

We implemented the strain and doping dependent Ge energy bandgap model in LASTIP and studied the stress engineering of Ge-on-Si lasers using the silicon nitride stressors. Side and top silicon nitride stressors were proposed and shown to be effective in reducing I_{th} and improving η_{wp}. Side stressors turned out to be a more efficient and easier way to increase η_{wp} than using top and side stressors together. With the side stressors only and geometry optimizations, a η_{wp} of 34.8%, and an I_{th} of 36 mA (J_{th} of 27 kA/cm^2) can be achieved with 1 ns defect limited carrier lifetime. These are tremendous improvements from the case without any stressors and geometry optimization, which has a η_{wp} of 2.07% and an I_{th} of 810 mA (J_{th} of 300 kA/cm^2), respectively. With a longer defect-limited minority carrier lifetime (better material quality), the performance of Ge lasers can be further improved. With $\tau_{p,n} = 10$ ns, an I_{th} of 4 mA (J_{th} of 3 kA/cm^2) and a η_{wp} of 43.8% could be achieved at 81 mA and an output power of 24 mW. These results give a strong support to the Ge-on-Si laser technology and provide effective ways to improve the Ge laser performance.

Acknowledgment

The authors would like to thank Crosslight Software, Inc., for providing the license of LASTIP, M. Lestrade from Crosslight Software for his assistance in LASTIP usage, and X. Li from the School of Electronic and Information Engineering, South China University of Technology, for helpful discussions.

Reference

[1] S. Chen *et al.*, "Electrically pumped continuous-wave III-V quantum dot lasers on silicon," *Nature Photon.*, vol. 10, pp. 307–311, 2016.
[2] Z. Zhou, B. Yin, and J. Michel, "On-chip light sources for silicon photonics," *Light, Sci. Appl.*, vol. 4, p. e358, 2015.
[3] J. Liu *et al.*, "Tensile-strained, n-type Ge as a gain medium for monolithic laser integration on Si," *Opt. Exp.*, vol. 15, no. 18, pp. 11272–11277, 2007.
[4] J. Liu, X. Sun, R. Camacho-Aguilera, L. C. Kimerling, and J. Michel, "Ge-on-Si laser operating at room temperature," *Opt. Lett.*, vol. 35, no. 5, pp. 679–681, 2010.
[5] R. E. Camacho-Aguilera *et al.*, "An electrically pumped germanium laser," *Opt. Exp.*, vol. 20, no. 10, pp. 11316–11320, 2012.
[6] R. Koerner *et al.*, "Electrically pumped lasing from Ge Fabry-Perot resonator on Si," *Opt. Exp.*, vol. 23, no. 11, pp. 14815–14822, 2015.
[7] S. Wirths *et al.*, "Lasing in direct-bandgap GeSn alloy grown on Si," in *Nature Photon.* vol. 9, pp. 88–92, 2015.
[8] M. Grydlik *et al.*, "Lasing from glassy Ge quantum dots in crystalline Si," *ACS Photon.*, vol. 3 no. 2, pp. 298–303, 2016.
[9] B. Dutt, D. S. Sukhdeo, D. Nam, B. M. Vulovic, Z. Yuan, and K. C. Saraswat, "Roadmap to an efficient germanium-on-silicon laser: Strain versus n-type doping," *IEEE Photon. J.*, vol. 4, no. 5, pp. 2002–2009, Oct. 2012.
[10] J. Michel *et al.*, "An electrically pumped Ge-on-Si laser," presented at the Opt. Fiber Commun. Conf., OSA Tech. Dig., Opt. Soc. Amer., Los Angeles, CA, USA, 2012, Paper PDP5A. 6.
[11] D. S. Sukhdeo, D. Nam, J. Kang, M. L. Brongersma, and K. C. Saraswat, "Direct bandgap germanium-on-silicon inferred from 5.7% ⟨100⟩ uniaxial tensile strain," *Photon. Res.*, vol. 2, no. 3, pp. A8–A13, Jun. 2014.
[12] G. Capellini *et al.*, "Tensile Ge microstructures for lasing fabricated by means of a silicon complementary metal-oxide-semiconductor process," *Opt. Exp.*, vol. 22, no. 1, pp. 399–410, 2014.
[13] D. Peschka *et al.*, "Robustness analysis of a device concept for edge-emitting lasers based on strained germanium," *Opt. Quantum Electron.*, vol. 48, p. 156, 2016.
[14] D. Nam *et al.*, "Strained germanium thin film membrane on silicon substrate for optoelectronics," *Opt. Exp.*, vol. 19, no. 27, pp. 25866–25872, 2011.
[15] X. Li, Z. Li, S. Li, L. Chrostowski, and G. Xia, "Design considerations of biaxially tensile-strained germanium-on-silicon lasers," *Semicond. Sci. Technol.*, vol. 31, 2016, Art. no. 065015.
[16] S. Pidin *et al.*, "A novel strain enhanced CMOS architecture using selectively deposited high tensile and high compressive silicon nitride films," in *Proc. IEEE Int. Electron Devices Meet.*, 2004, pp. 213–216.
[17] R. E. Camacho-Aguilera, "Ge-on-Si LASER for silicon photonics," Ph.D. dissertation, Dept. Mater. Sci. Eng., Mass. Inst. Technol., Cambridge, MA, USA, 2013.

[18] D. J. Paul, "Si/SiGe heterostructures: From materials and physics to devices and circuits," *Semicond. Sci. Technol.*, vol. 19, no. 10, pp. R75–R108, Oct. 2004.
[19] K. Brunner, "Si/Ge nanostructures," *Rep. Prog. Phys.*, vol. 65, no. 1, pp. 27–72, Jan. 2002.
[20] R. Camacho-Aguilera, Z. Han, Y. Cai, L. C. Kimerling, and J. Michel, "Direct band gap narrowing in highly doped Ge," *Appl. Phys. Lett.*, vol. 102, no. 15, p. 152106, Apr. 2013.
[21] Y. Cai *et al.*, "Analysis of threshold current behavior for bulk and quantum well germanium laser structures," *IEEE J. Sel. Topics Quantum Electron.*, vol. 19, no. 4, Jul. 2013, Art. no. 1901009.
[22] D. S. Sukhdeo, S. Gupta, K. C. Saraswat, B. Dutt, and D. Nam, "Impact of minority carrier lifetime on the performance of strained germanium light sources," *Opt. Commun.*, vol. 364, pp. 233–237, 2016.
[23] R. E. Camacho-Aguilera, "Monolithically-integrated Ge CMOS laser," in *Proc. SPIE 9010, Next-Generation Opt. Netw. for Data Centers and Short-Reach Links, 90100H*, vol. 9010, Feb. 2014. doi:10.1117/12.2044057.
[24] R. Newman and W. W. Tyler, "Effect of impurities on free-hole infrared absorption in p-type germanium," *Phys. Rev.*, vol. 105, no. 3, pp. 885–886, Feb. 1957.
[25] S. L. Chuang, *Physics of Photonic Devices*, 1st ed. New York, NY, USA: Wiley, 1995, ch. 2, sec. 6.
[26] R. Geiger *et al.*, "Excess carrier lifetimes in Ge layers on Si," *Appl. Phys. Lett.*, vol. 104, p. 062106, 2014.
[27] D. Nam, J. Kang, M. L. Brongersma, and K. C. Saraswat, "Observation of improved minority carrier lifetimes in high quality Ge-on-insulator using time-resolved photoluminescence," *Opt. Lett.*, vol. 39, no. 21, pp. 6205–6208, 2014.
[28] F. Cai, D. H. Anjum, X. Zhang, and G. Xia, "Study of Si-Ge interdiffusion with phosphorus doping," *J. Appl. Phys.*, vol. 120, p. 165108, 2016.
[29] F. Cai, Y. Dong, Y. H. Tan, C. S. Tan, and G. Xia, "Enhanced Ge-Si interdiffusion in high phosphorus-doped germanium on silicon," *Semicond. Sci. Technol.*, vol. 30, 2015, Art. no. 105008.
[30] L. Buchaillot, E. Farnault, M. Hoummady, and H. Fujita, "Silicon nitride thin films Young's modulus determination by an optical non destructive method," *Jpn. J. Appl. Phys.*, vol. 36, p. L794, 1997.